

The load carrying capacity of textured sliding bearings with elastic deformation



Binbin Su^a, Lirong Huang^b, Wei Huang^a, Xiaolei Wang^{a,*}

^a College of Mechanical and Electrical Engineering, Nanjing University of Aeronautics and Astronautics, Nanjing, People's Republic of China

^b School of Mechanical and Electrical Engineering, Jiangxi University of Science and Technology, Ganzhou, People's Republic of China

ARTICLE INFO

Keywords:

Elastic deformation
Surface texture
Hydrodynamic
Load carrying capacity

ABSTRACT

A two-dimensional elastohydrodynamic numerical simulation is conducted for surface textured sliding bearings with relatively soft material. The pressure distribution in the film and the elastic deformation of the textured surfaces are obtained through a simultaneous solution of the two-dimensional Reynolds equation and the equation of the elasticity for the textured surface. The results show that the small elastic deformation has significant influence on the load carrying capacity and pressure distribution, and leads to a drastic decrease in load capacity at thin film hydrodynamic lubrication. A parametric analysis is conducted to obtain the optimal surface texture parameters in term of load carrying capacity.

1. Introduction

Surface texturing is proved to be an efficient method to enhance the tribological properties of lubricated sliding bearings and mechanical seals both experimentally and theoretically [1–6]. It is widely accepted that the advantageous effect of surface texturing on fluid lubrication properties is attributed to the creation of an additional hydrodynamic lift, which primarily depends on shape, density, depth and pattern of dimples [7].

Most of texturing parameters that affect the overall contact lubricant performance have been extensively investigated through theoretical method. In order to obtain the optimal load capacity of the sliding bearing, Etsion et al. [1,8] systematically investigated the effect of texturing parameters, including diameter, texture density and the dimple depth over diameter ratio. In the more generalized optimization studies by Nanbu [9] and Rahmani [10], infinitely long parallel sliders with different texture bottom shapes were analysed. Yu et al. [11] developed a theoretical model to investigate the effect of textural shapes and orientations on hydrodynamic pressure between conformal contact, ellipses placed perpendicular to sliding direction showed the best performance of load-carrying capacity and this was experimentally proved in a later study [12]. Han and Ge [13] numerically studied the hydrodynamic lubrication properties of the textured surface with asymmetric micro-dimples and found the asymmetric micro-dimples can obtain larger load-carrying capacity than a symmetric rectangular micro-dimples. Khonsari et al. [14,15] investigated fully textured parallel slider bearings by developing a numerical

texture shape optimization approach based on the Successive Quadratic Programming (SQP) algorithm and they found that chevron-like shape is the optimal dimple shapes.

Experimental researches also have been extensively conducted. Etsion et al. [16,17] experimentally validated the optimal texturing parameters obtained by their previous numerical modeling. Wang et al. [18,19] experimentally studied surface textured silicon carbide sliding in water, and found out the optimal texture area density in term of friction reduction and load carrying capacity respectively. Meng et al. [20,21] directly observed the cavitation phenomenon inside surface textured thrust bearings by using high-speed camera, they found that cavitation shape and area varied with texture patterns, and confirmed that Jakobsson - Floberg - Olsson (JFO) models are more valid for the prediction of cavitation morphology compared with Reynolds model.

In aforementioned researches, surface textures were applied mostly for the stiff materials such as steel and ceramics, which are usually assumed as rigid materials in simulation. On the other hand, relatively soft materials become increasingly used in tribo-contacts, such as joint prosthesis and engineering seals. Optimization is more complicated when the materials became softer. Zhang et al. [22,23] studied the effect of surface texture on friction reduction between the contact of Ultra High Molecular Weight Polyethylene (UHMWPE) and steel, the optimal dimples area density depended on whether the dimples were on the surface of UHMWPE or steel. The dimples textured on the surface of UHMWPE with an area density ranging from 16% to 30% can effectively reduce friction, while the optimal density was in the range of 5–15% if the dimples are fabricated on the surface of steel.

* Corresponding author.

E-mail address: wxl@nuaa.edu.cn (X. Wang).

Nomenclature

h	film thickness
h_0	initial film thickness
h_p	dimple depth
p	local pressure of fluid film
p_0	ambient atmospheric pressure
q	total mass flow rate
q_c	Couette mass flow rate
q_p	Poiseuille mass flow rate
r_p	radius of the dimple
ρ	density of lubricant
ρ_0	density of lubricant at $p=p_0$
$\bar{\rho}$	dimensionless density of lubricant
η	viscosity of lubricant
η_0	viscosity of lubricant at $p=p_0$
$\bar{\eta}$	dimensionless viscosity of lubricant
x	coordinate along with sliding direction
y	coordinate perpendicular to sliding direction
s, t	local coordinates
S, T	dimensionless local coordinates
δ	elastic displacement of textured surface

ν_1, ν_2	Poisson's ratio of contact surfaces
α	pressure-viscosity coefficient of lubricant
A	contact area
D_{ij}^{kl}	deformation matrix
E_1, E_2	Young's modulus of contact surfaces
E'	equivalent elastic modulus of contact surfaces
P	dimensionless local pressure of fluid film
P_{av}	dimensionless average pressure
H	dimensionless film thickness
L	side length of imaginary square cell
U	sliding velocity
X	dimensionless coordinate along with sliding direction
Y	dimensionless coordinate perpendicular to sliding direction
(X_0, Y_0)	rupture local of oil film
S_a	area density
W	dimensionless load carrying force
Ω	dimple region
Ω'	total computational domain of textured plane
Δ	dimensionless elastic deformation of textured surface.

Wang [24] attributed this difference to the deformation of the soft material, and proposed that the deformation should also be responsible for the difference of the optimal values of area density between that obtained by theoretical models and that by experiments.

In order to accurately predict the performance of the surface textured slider bearings with relative soft materials, the effect of elastic deformation should be included in the numerical simulation. Etsion [25] included the effect of elastic deformation in modeling of surface texturing in soft elasto-hydrodynamic lubrication. Yagi et al. [26,27] developed an elasto-hydrodynamic numerical simulation which takes into account elastic deformation of the bounding surface for one-dimensional step bearings, and the results showed that a small elastic deformation of less than 100 nm leads to a sharp decline in lubricant pressure from 120 MPa to 5 MPa. Shinkarenko et al. [28,29] developed a numerical model for rubber seal against rigid rod, either of the surfaces was textured. The pressure distribution in fluid film and the elastic deformation of the elastomer were obtained by ANSYS software. The elastic deformation was showed to exceed the initial clearance by almost threefold and became the key component of lubricant film thickness.

In the present study, a two-dimensional elasto-hydrodynamic numerical simulation that takes into account the elastic deformation of the surface and the viscosity-pressure effect of the lubricant is conducted for surface textured sliding bearings. The bearings consist of textured polymer materials and smooth steel. The numerical modeling investigates the influence of elastic deformation on lubrication property emphatically, and the results are compared with those obtained from the rigid solution which ignores the small elastic deformation in thin film lubrication. Meantime, a parametric analysis is conducted to obtain the optimal surface texture parameters in term of load carrying capacity.

2. The model

The schematic diagram of surface textured sliding bearings is presented in Fig. 1. The numerical model consists of a steel plate with a smooth surface sliding at constant velocity of U relatively to a stationary polymer plate with surface texture in form of dimples. The two surfaces are separated by a layer of lubricant with initial thickness of h_0 .

Fig. 1(a) presents a geometrical model of the upper stationary

textured surface. The dimples in the form of cylinder are uniformly distributed on the surface with an area density S_a . Each cylindrical dimple has a base radius r_p and depth h_p (see Fig. 1b) and is located in the center of an imaginary square cell of sides $L \times L$. The dimple area density and radius are related to the square area by the following formula :

$$L = r_p \sqrt{\frac{\pi}{S_a}} \tag{1}$$

The total computational domain of the upper fixed textured plane in the simulation model lie in a square cell of sides $3L \times 3L$. The x - y coordinates are established on the upper stationary textured plane as

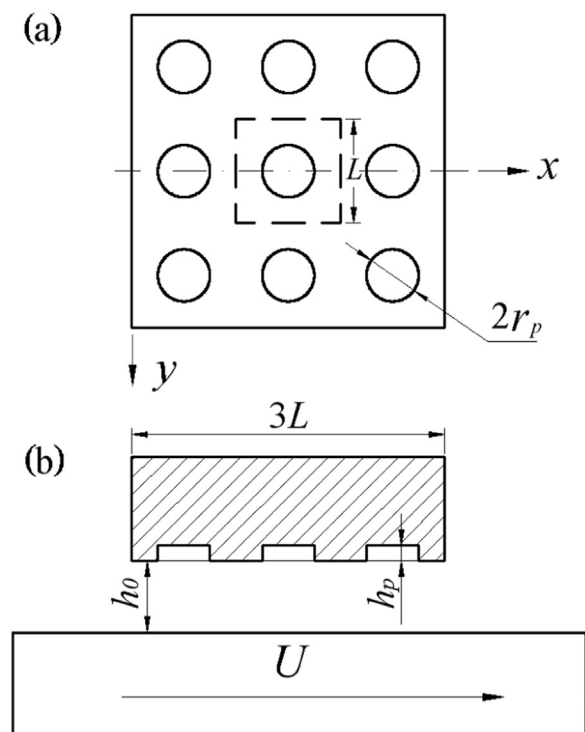


Fig. 1. Schematic illustration of the model: (a) geometry of textured surface; (b) working schematic of textured sliding bearing.

show in Fig. 1(a).

The two-dimensional Reynolds equation for the local pressure in fluid film is expressed as follows:

$$\frac{\partial}{\partial x} \left(\frac{\rho h^3}{\eta} \frac{\partial p}{\partial x} \right) + \frac{\partial}{\partial y} \left(\frac{\rho h^3}{\eta} \frac{\partial p}{\partial y} \right) = 6U \frac{\partial}{\partial x} (\rho h) \quad (2)$$

where x and y are Cartesian coordinates (see Fig. 1); h is local film thickness; p is the local pressure in lubricant film; ρ and η are the density and viscosity of lubricant respectively; U is the relative velocity between contact surfaces. A dimensionless form of the Reynolds equation can be written as follows:

$$\frac{\partial}{\partial X} \left(\frac{\bar{\rho} H^3}{\bar{\eta}} \frac{\partial P}{\partial X} \right) + \frac{\partial}{\partial Y} \left(\frac{\bar{\rho} H^3}{\bar{\eta}} \frac{\partial P}{\partial Y} \right) = \Lambda \frac{\partial}{\partial X} (\bar{\rho} H) \quad (3)$$

where

$$X = \frac{x}{r_p}, Y = \frac{y}{r_p}, H = \frac{h}{h_0}, P = \frac{p}{p_0}, \bar{\rho} = \frac{\rho}{\rho_0}, \bar{\eta} = \frac{\eta}{\eta_0}, \Lambda = \frac{6U\eta_0 r_p}{h_0^2 p_0} \quad (4)$$

during the above normalization of the problem parameters, r_p is dimple radius; h_0 is the initial film thickness as showed in Fig. 1(b); p_0 is ambient atmospheric pressure; ρ_0 and η_0 are the density and viscosity of lubricant at $p=p_0$, respectively.

The film thickness h , considering the elastic displacement of upper textured surface, can be formulized as follows:

$$h = \begin{cases} h_0 + h_p + \delta & (x, y) \in \Omega' \\ h_0 + \delta & (x, y) \notin \Omega' \end{cases} \quad (5)$$

where δ is the elastic displacement of upper fixed textured surface, Ω' represents dimple region of the upper fixed textured plane.

The elastic deformation of the textured polymer surface can be mathematically derived according to Boussinesq's analytical model [30] based on the assumption of semi-infinite body theory and is expressed as follows:

$$\delta(x, y) = \frac{2}{\pi E'} \iint_{\Omega} \frac{p(s, t)}{\sqrt{(x-s)^2 + (y-t)^2}} ds dt \quad (6)$$

$$\frac{1}{E'} = \frac{(1-\nu_1^2)}{E_1} + \frac{(1-\nu_2^2)}{E_2} \quad (7)$$

where E' is equivalent elastic modulus, s and t are local coordinates, E and ν are Young's modulus and Poisson's ratio of the contact surfaces respectively, Ω represents total computational domain of the upper fixed textured surface.

The dimensionless forms of the above equations then can be expressed as follows:

$$H = \begin{cases} 1 + K + \Delta & (X, Y) \in \Omega' \\ 1 + \Delta & (X, Y) \notin \Omega' \end{cases} \quad (8)$$

$$\Delta = \frac{\delta}{h_0} = \frac{2r_p p_0}{\pi E' h_0} \iint_{\Omega} \frac{P(S, T)}{\sqrt{(X-S)^2 + (Y-T)^2}} dS dT \quad (9)$$

$$K = \frac{h_p}{h_0} \quad (10)$$

The dimensionless density and viscosity of lubricant developed by Dowson et al. [31,32] are expressed as follows:

$$\bar{\rho} = \frac{\rho}{\rho_0} = 1 + \frac{0.6p_0 P}{1 + 1.7p_0 P} \quad (11)$$

$$\bar{\eta} = \frac{\eta}{\eta_0} = \exp(\alpha p_0 P) \quad (12)$$

where α is the pressure-viscosity coefficient of lubricant with the unit of GPa.

The dimensional equations of the mass flow rate are expressed as

follows:

$$q = q_c + q_p \quad (13)$$

$$q_c = \rho U \frac{h}{2}, \quad q_p = -\rho \frac{h^3}{12\eta} \frac{dp}{dx} \quad (14)$$

where q is the total mass flow rate, q_c and q_p are the Couette and poiseuille mass flow rate, respectively.

The dimensionless load carrying force can be obtained by integrating the local hydrodynamic pressure over contact area as follows:

$$W = \iint_{\Omega} P(X, Y) dXdY \quad (15)$$

The dimensionless average pressure is chosen to measure the load carrying capacity of sliding bearings and evaluate the hydrodynamic effect of the surface texture. In the present study it can be expressed as:

$$P_{av} = \frac{W}{A} \quad (16)$$

where A stands for contact area.

The above dimensionless equations are discretized on a uniform spatial grid and simultaneously solved on the basis of the finite difference method. Fig. 2 presents a flowchart of the numerical procedure for the simultaneous iterative solution of the hydrodynamic lubrication problem and the elastic deformation. With the help of working condition parameters and initial value of film thickness and pressure, a first approximated hydrodynamic pressure is obtained by the solution of the Reynolds equation; the obtained pressure is used for the calculation of the elastic deformation, density and viscosity; after that, the film thickness is renewed by incorporating the obtained elastic

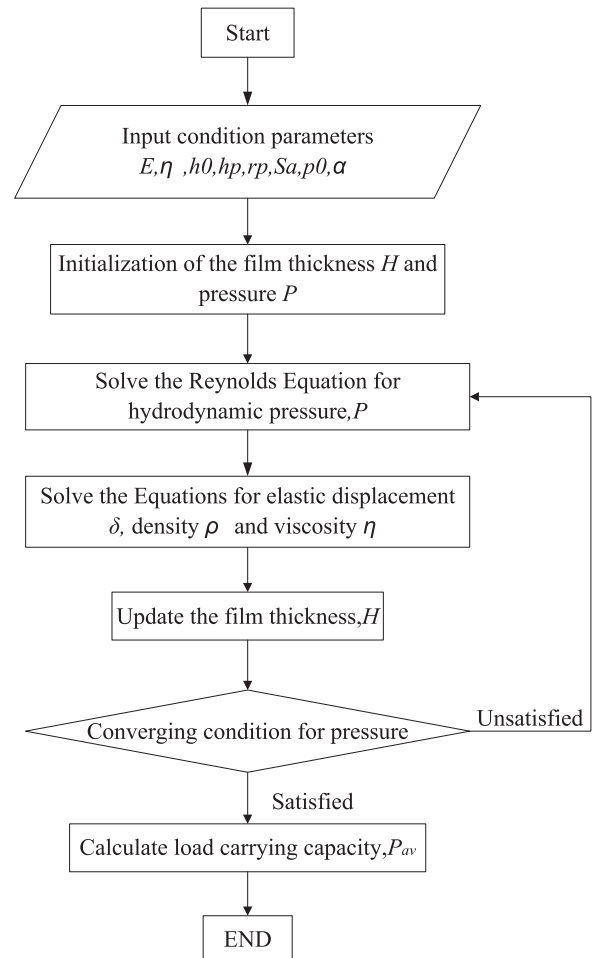


Fig. 2. Flow chart of the calculation process.

deformation and then returned to Reynolds equation; this iterative process is repeated until a desired convergence of pressure is achieved.

After discretization of Reynolds equation, the Gauss-Seidel iteration with successive over relaxation (SOR) is applied to the set of non-linear algebraic equations, the converging condition is taken as follows:

$$P_{i,j}^{k+1} = P_{i,j}^k + \beta(\bar{P}_{i,j}^{k+1} - P_{i,j}^k) \tag{17}$$

where β is the relaxation factor and $\beta=1.75$ is chosen to obtain a fast convergence, $P_{i,j}^k, P_{i,j}^{k+1}$ are the pressure values at iterative step k and $k+1$, $\bar{P}_{i,j}^{k+1}$ is the temporary values at step $k+1$.

At the same time, the V-cycle style of multigrid method is used to accelerate the SOR iteration and improve the numerical stability. Fig. 3 shows the schematic diagram of V-cycle multigrid with four levels applied in this study. The top level is meshed by the finest grid of 169×169 nodes whereas bottom level has the coarsest grid of 22×22 nodes, intermediate levels are meshed by grid nodes of 85×85 and 43×43 , respectively. The downward portion of the V-cycle presents the restriction process and the upward portion presents the prolongation process, with restriction operator and prolongation operator attached to corresponding side. N0, N1 and N2 represent the iterations of SOR in current mesh layers, they are respectively assigned to the values of 15, 2 and 1 in present study. More details and theory about multigrid method is presented in [33,34].

The V-cycle process is repeated until the following convergence criteria reached:

$$\left\| \frac{P_{i,j}^{n+1} - P_{i,j}^n}{P_{i,j}^n} \right\| \leq Err \tag{18}$$

where $P_{i,j}^n, P_{i,j}^{n+1}$ are the pressure values from previous and current V-cycle iteration, respectively. Err is the error tolerance, taken as 1.0×10^{-5} here.

The Boussinesq's integral Eq. (6) is solved by an improved numerical technique for computing surface elastic deformation proposed by Wen et al. [35] Through this method, the deformation of every node can be expressed as a linear combination of the nodal pressures whose coefficients can be combined into a deformation matrix just as follows:

$$\delta_{kl} = \frac{2}{\pi E'} \sum_i \sum_j D_{ij}^{kl} P_{ij} \tag{19}$$

where δ_{kl} is nodal elastic deformation, D_{ij}^{kl} is the deformation matrix which only dependent on the geometric factors of the grids, therefore all the values of must be completely computed only once and the elastic deformation can be calculated repeatedly by only applying the Eq. (19). For more detail on the calculation of the deformation matrix, the reader is referred to reference [35].

The focus of our work is the effect of elastic deformation, which is also the major contribution of our work. In order for the time-saving steady computational program and simplicity of implementation, the numerical simulation employs Reynolds cavitation boundary condition which is not mass conserving. The boundary conditions for discrete Reynolds equation and the Reynolds boundary condition for the cavitation in dimensionless form are as follows:

Ambient pressure at the inlet, outlet and both sides of the textured sliding plane bearing:

$$P(X = 0, Y) = P\left(X = \frac{3L}{r_p}, Y\right) = P\left(X, Y = \pm \frac{3L}{2r_p}\right) = 1 \tag{20}$$

The pressure in cavitation regions is set value of P_0 (atmospheric pressure) according to Reynolds cavitation condition:

$$P(X_0, Y_0) = 1 \text{ and } \frac{\partial P(X_0, Y_0)}{\partial X} = \frac{\partial P(X_0, Y_0)}{\partial Y} = 0 \tag{21}$$

where (X_0, Y_0) presents the rupture location of hydrodynamic lubricat-

ing film. In order to determine the cavitation boundary, the nodal pressure is set to 1 if its value of pressure is less than 1 during the iteration process.

3. Results and discussions

All results of the indexes that evaluate the lubrication properties in present study are calculated from the center square cell of sides $L \times L$ (shown by the dashed line in Fig. 1a) in order to mitigate the influence of boundary condition. The indexes mainly include dimensionless average pressure P_{av} , average deformation δ_{av} , and minimum film thickness h_{min} .

Some basic fixed parameters used in present study are listed in Table 1. Paraffinic oil plays the role of lubricant. Other parameters such as initial film thickness (h_0), area density (S_a), ratio of dimple depth to dimple diameter ($\lambda = h_p / (2 \times r_p)$) and sliding velocity (U) are varied during the investigation.

3.1. Dimensionless average pressure P_{av}

Fig. 4 shows the effect of initial film thickness h_0 on the values of dimensionless average pressure P_{av} . For both the rigid solution and elastohydrodynamic (EHD) solution, the values of dimensionless average pressure decrease with the growth of initial film thickness and tend to become stable until $h_0 \geq 2.5 \mu\text{m}$. However, the decrease of dimensionless average pressure calculated from the rigid solution is much more sharp than that of EHD solution, especially in thin film hydrodynamic lubrication ($h_0 < 1 \mu\text{m}$). As the initial film thickness decreases, the difference in dimensionless average pressure between the rigid solution and EHD solution becomes increasingly significant, for instance, the value of P_{av} obtained from the rigid solution reaches the value of 26.58 at $h_0 = 0.1 \mu\text{m}$, outperforming that of the UHMWPE under EHD solution by a factor of 15.8. At the same time, the figure also presents the effect of the surface's elastic modulus on dimensionless average pressure through comparing the result of UHMWPE and PE (Poly Ethylene). The value of P_{av} obtained from the rigid solution outperform that of the PE under EHD solution by a factor of 45.8 at $h_0 = 0.1 \mu\text{m}$, the lower the elastic modulus of the surface, the smaller the value of the dimensionless average pressure.

As show in Fig. 4, the dimensionless average pressure P_{av} of the PE under EHD solution does not vary significantly with the increase of initial film thickness. Consequently, the EHD solutions in the following study are all conducted for the tribo-contact between UHMWPE and steel.

Fig. 5 shows the dimensionless average pressure P_{av} for various sliding velocity U at thin film thickness $h_0 = 0.1 \mu\text{m}$. With the growth of sliding velocity, the dimensionless average pressure for EHD solution has a trend of slow increase while that value for rigid solution proportionately increases in a high rate, which results in the expanding differences of the dimensionless average pressure between the two different solutions.

Fig. 6 describes the dimensionless average pressure P_{av} for various area density S_a at thin film thickness $h_0 = 0.1 \mu\text{m}$. It can be seen that the

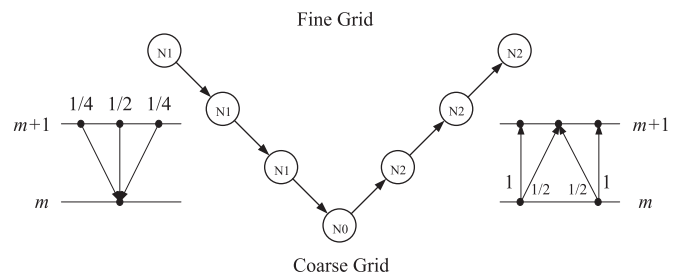


Fig. 3. Schematic diagram of V-cycle multigrid with four levels.

Table 1
Basic parameters.

Item	Value
Elastic modulus E	0.85 GPa (UHMWPE)
	0.172 GPa (PE (Poly Ethylene))
	210 GPa (steel)
Poisson's ratio ν	0.46 (UHMWPE)
	0.439 (PE (Poly Ethylene))
	0.3 (steel)
Radius of dimple r_p	50 μm
Viscosity of lubricant η_0	0.061 Pa s
Density of lubricant ρ_0	900 kg/m ³
Pressure-viscosity coefficient α	$2 \times 10^{-8} \text{ m}^2 \text{ N}^{-1}$

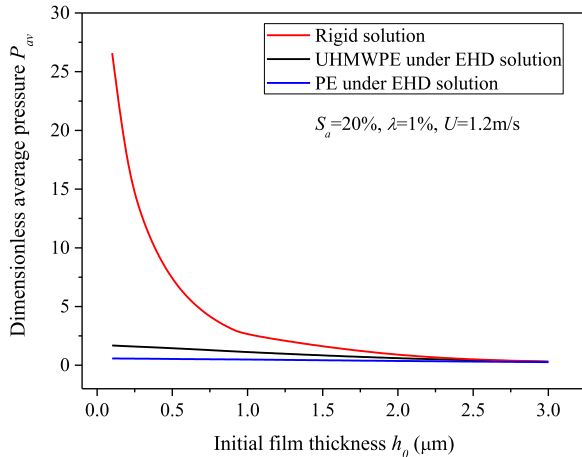


Fig. 4. Effect of initial film thickness h_0 on the dimensionless average pressure P_{av} at $S_a=20\%$, $\lambda=1\%$ and $U=1.2 \text{ m/s}$.

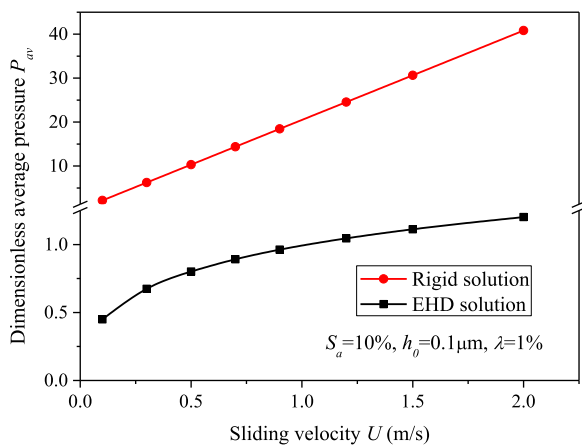


Fig. 5. Effect of the sliding velocity U on the dimensionless average pressure P_{av} at $S_a=10\%$, $h_0=0.1 \mu\text{m}$ and $\lambda=1\%$.

dimensionless average pressure for rigid solution remains greater than that for EHD solution during the change of the area density. For rigid solution, the change trend firstly increase and then descend with the increasing of the area density; dimensionless average pressure reaches its peak point at area density $S_a=30\%$. For EHD solution, the dimensionless average pressure increases slightly with the growth of the area density within the range of 10–30% and then tend to remain stable.

Fig. 7 presents the effect of initial film thickness h_0 on the optimal area density S_a (circled by the dashed line) for rigid and EHD solution. The change of dimensionless average pressure P_{av} with area density S_a becomes increasingly remarkable as the initial film thickness h_0

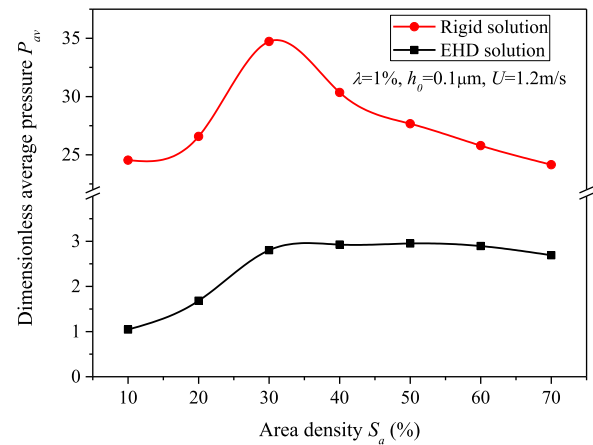


Fig. 6. Effect of area density S_a on the dimensionless average pressure P_{av} at $\lambda=1\%$, $h_0=0.1 \mu\text{m}$ and $U=1.2 \text{ m/s}$.

decreases. Meanwhile, dimensionless average pressure P_{av} reach its peaks under different area density S_a . For EHD solution (see Fig. 7(b)), when $h_0 \leq 0.5 \mu\text{m}$, the maximum P_{av} occurs at $S_a=50\%$, in the range of $h_0=0.5-1 \mu\text{m}$, the maximum P_{av} happens at $S_a=40\%$, while for $h_0 > 1 \mu\text{m}$, the maximum P_{av} is obtained at $S_a=20\%$. While for rigid solution (see Fig. 7(a)), the maximum P_{av} all gain at $S_a=10\%$ except that when $h_0=0.1 \mu\text{m}$, which maximum acquires at $S_a=30\%$.

Fig. 8 presents the effect of the ratio of dimple depth to dimple diameter λ on dimensionless average pressure P_{av} when either the dimple depth or its diameter is varied. As shown clearly by the graph, in the case of EHD solution, the dimensionless average pressure increases slightly with the growth of the ratio λ , whereas the opposite tendency of decreasing dramatically is displayed for rigid solution.

The finding to be emphasized most in Figs. 4–8 is that elastic deformation can result in a drastic reduction in the load carrying capacity of textured sliding bearings. This can be explained in two ways according to Yagi's analysis in previous studies [26,27]. On one hand, the elastic deformation diminishes the step film shape in the convergent part of the textures, especially the bottom of the textures become divergent wedges, circled by the dashed line and show in Fig. 9. On the other hand, the Poiseuille flow rate is proportional to the third power of the film thickness film through the magnitude of $\rho h^3/\eta$ according to Eq. (14), elastic deformation makes the resistance to the Poiseuille flow reduce significantly because of the overall increase in film thickness compared with the Rigid solution, just as show in Fig. 9.

It can be seen clearly that the emergence of elastic deformation leads the load carrying capacity of textured sliding bearings to become insensitive to the texture parameters (Figs. 6 and 8) and operation condition (Fig. 5). Meanwhile, the appearance of the elastic deformation is also found to change the optimal values of the area density S_a and the ratio of dimple depth to its diameter λ compared with the Rigid solutions (Figs. 6–8).

It should be noticed in Fig. 8 that the dimensionless average pressure P_{av} changes in the opposite trend with the increase of dimple depth over diameter ratio for the Rigid and EHD solutions no matter when either the dimple depth or its diameter is varied. In the Rigid solution, the dimensionless average pressure P_{av} decreases dramatically with the increase of dimple depth over diameter ratio, which is in good agreement with those results obtained by Etsion [36]. In the EHD solution, deep dimple maybe good for the retention of film shape in the convergent part of the textures after elastic deformation, so that deep dimple is more effective for the pressure generation when taking elastic deformation into consideration.

3.2. Average elastic deformation δ_{av}

As showed above, elastic deformation of the soft textured surface

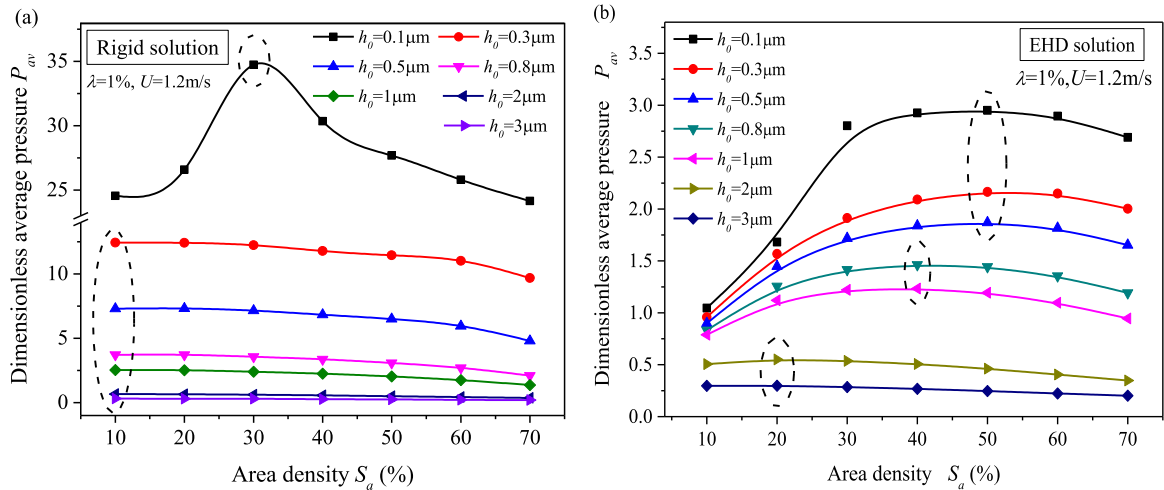


Fig. 7. Effect of initial film thickness h_0 on optimal area density S_a at $\lambda=1\%$ and $U=1.2$ m/s.

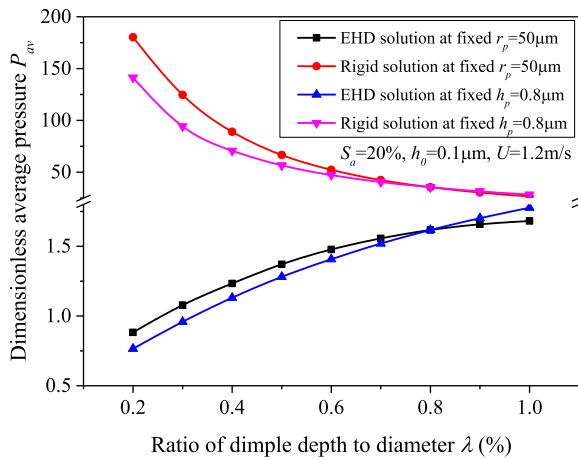


Fig. 8. Effect of the ratio of dimple depth to dimple diameter on the dimensionless average pressure P_{av} at $S_a=20\%$, $h_0=0.1$ μm and $U=1.2$ m/s.

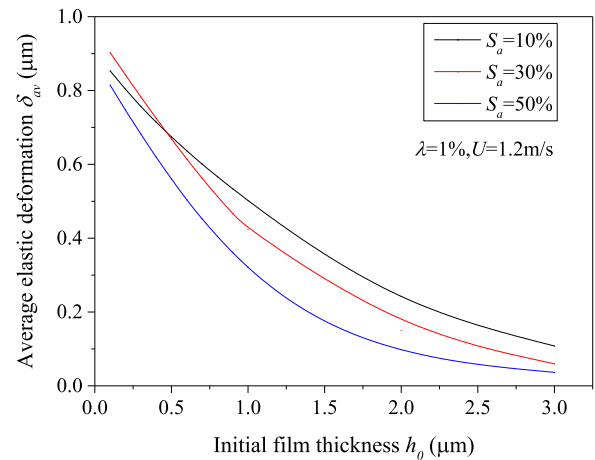


Fig. 10. Effect of the initial film thickness h_0 on the average elastic deformation δ_{av} for various S_a at $\lambda=1\%$ and $U=1.2$ m/s.

has a significant influence on dimensionless pressure P_{av} , it is necessary to study the deformational degree described by average elastic deformation δ_{av} , which is the mean value of deflection in the center square cell.

Fig. 10 shows the average elastic deformation δ_{av} of EHD solution for various initial film thickness h_0 at $\lambda=1\%$ and $U=1.2$ m/s. The average elastic deformation δ_{av} increases dramatically as initial film thickness h_0 decreases and reaches a value of about 0.85 μm at $h_0=0.1$ μm . The values of average deformation δ_{av} become greater than the initial film thickness h_0 while the thin film lubrication h_0 is less than 0.5 μm .

Fig. 11(a) and (b) respectively presents the values of average elastic deformation δ_{av} for various area density S_a and ratio of dimple depth to diameter λ at thin film thickness $h_0=0.3$ μm . The effect of area

density S_a on average elastic deformation δ_{av} presents the parabolic changing tendency and reaches its maximum values near $S_a=20\%$, just as shown in Fig. 11(a). The average elastic deformation first increases moderately and then keeps constant value with the increase of the ratio of dimple depth to its diameter λ , as shown in Fig. 11(b).

The pressure produced in lubricant film is transmitted to the tribo-contacting surfaces, resulting in elastic deformation of the soft textured surface. The relationship between the elastic deformation and lubricant pressure is reflected in Eq. (6). Consequently, the variation tendencies of average elastic deformation along with texture parameters are roughly coincident with that of dimensionless average pressure in the EHD solution. Those can be confirmed easily through the comparisons between Figs. 4 and 10, Figs. 7(b) and 11(a), Figs. 8 and 11(b), respectively.

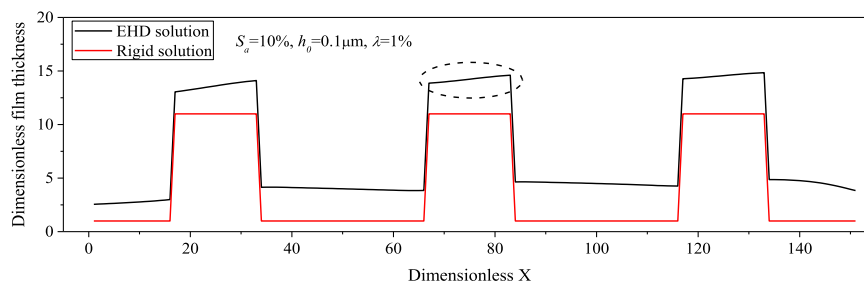


Fig. 9. Distribution of dimensionless film thickness along the x coordinate axis.

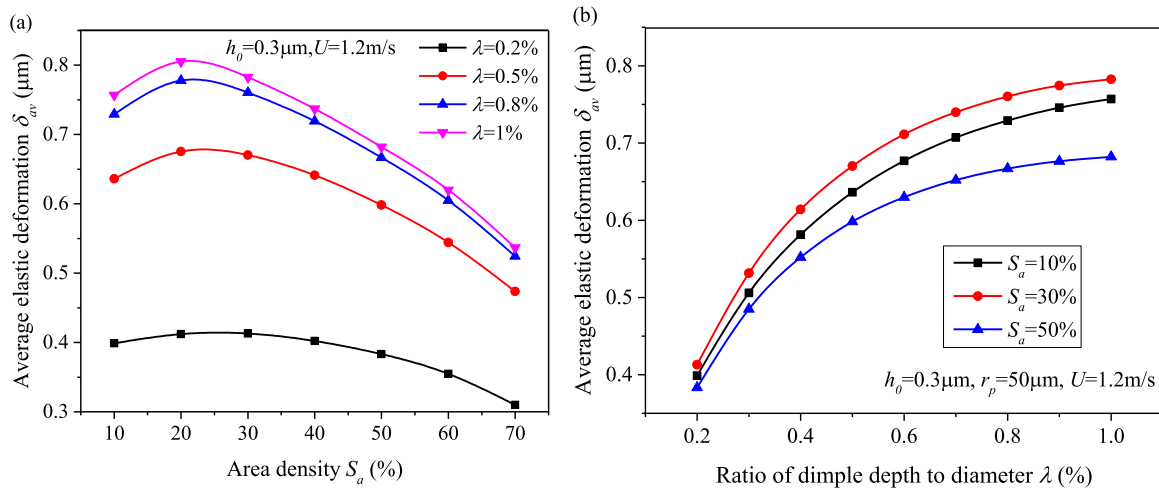


Fig. 11. Effect of the parameters of the surface texture on the average elastic deformation δ_{av} at thin film thickness $h_0=0.3\mu\text{m}$ and $U=1.2\text{m/s}$.

3.3. Minimum film thickness h_{min}

Since the elastic deformation of surface directly affects the lubricant film thickness, the minimum lubricating oil film thickness including the surface elastic deformation, h_{min} , are obtained from the center square cell of sides $L \times L$ (shown by the dashed line in Fig. 1a).

Fig. 12 shows the values of minimum film thickness h_{min} for various initial film thickness h_0 at $S_a=10\%$, $\lambda=1\%$ and $U=1.2\text{m/s}$. The minimum film thickness h_{min} for EHD solution reaches as high as $0.81\mu\text{m}$ at $h_0=0.1\mu\text{m}$, outperforming that values of the rigid solution by a factor of 7. With the increase of initial film thickness, the distinction in minimum film thickness between EHD solution and rigid solution becomes more and more subtle. Elastic deformation of the textured surface helps to increase the film thickness. The variation trend of minimum film thickness for EHD solution is similar to that obtained by Yagi [27], and it can be inferred that the elastic deformation of the surface becomes the major component of the film thickness h in the case of thin film lubricant.

Fig. 13(a) and (b) respectively presents the values of minimum film thickness h_{min} for various area density S_a and ratio λ of the surface texture. Just as demonstrated in Fig. 12, the elastic deformation of the surface becomes the major component of the film thickness h for EHD solution in the case of thin initial film lubrication. Consequently, the variation tendency of the minimum film thickness h_{min} over area density S_a and ratio λ display highly similarity to that of average elastic deformation δ_{av} (see Fig. 11(a) and (b) respectively).

3.4. Distribution of dimensionless pressure and elastic deformation

Fig. 14 shows the pressure distribution at the sliding bearings interface and the corresponding elastic deformation distribution at the textured UHMWPE surface. The black circles in the figure represent the position of dimples. It demonstrates a gradual pressure buildup along the lubricant flow direction which is from left to right in pictures, reaching a maximum at the dimple rear end. Elastic deformation of the textured surface mainly occurs across the zone of pressure buildup and reaches a maximum around the rightmost rim of dimple.

Fig. 15 depicts the distorted textured surface of the center square cell at $h_0=0.1\mu\text{m}$, $S_a=20\%$, $\lambda=1\%$ and $U=1.2\text{m/s}$. The lubricant flows along X-coordinate axis. The original position of the top surface and dimple bottom locate at $Z=0$ and $Z=-1\mu\text{m}$, respectively. Right picture is the section cuts of trimetric view. It can be seen that elastic deformation occurs not only on the surface but also at the bottom of dimple. It is this elastic deformation that produces the difference in pressure distribution and load carrying capacity. The initial flat surfaces start to sink under the action of lubricant pressure and the

most serious sunk part is at the dimple rear end, which corresponds with the distribution of elastic deformation showed in Fig. 14.

Fig. 16 presents the effect of initial film thickness h_0 on the dimensionless pressure and corresponding elastic deformation distribution at $S_a=20\%$, $\lambda=1\%$, and $U=1.2\text{m/s}$. The dimensionless pressure, as well as elastic deformation, has similar distribution for various initial lubricant film thickness h_0 . Meanwhile, the pressure levels and elastic deformation degrees decrease moderately as initial film thickness h_0 increases.

Fig. 17 describes the distributions of dimensionless pressure and elastic deformation for various depth-diameter ratio λ at $h_0=0.1\mu\text{m}$, $S_a=20\%$, and $U=1.2\text{m/s}$. When dimple is shallow ($\lambda=0.2\%$), low pressure region spreads out through the whole calculating cell, and high pressure compress in a small piece of the convergent region around the right rim of dimple (see Fig. 16(a)). As dimples become increasingly deep, the region of pressure build-up increases by extending all around, and low pressure area changes in opposite directions at the same time (see Fig. 16(b) and (c)). The distribution shapes of elastic deformation are similar for various dimple depth-diameter ratio λ , while the level of elastic deformation rises as depth-diameter ratio λ increases.

Fig. 18 displays the effect of dimple area density S_a on the distribution of dimensionless pressure and elastic deformation at $h_0=0.1\mu\text{m}$, $\lambda=1\%$, and $U=1.2\text{m/s}$. Just as shown in the figure, the whole quadrate cell tends to be symmetrically divided by the areas of low and high lubricant pressure as the growth of area density S_a . At the same time, the elastic deformation becomes smaller at higher area

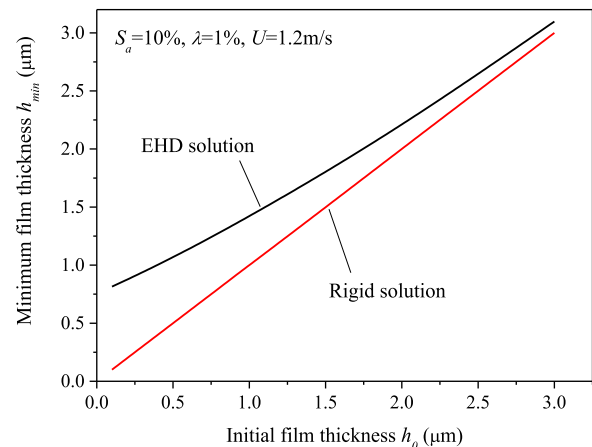


Fig. 12. Effect of the initial film thickness h_0 on the minimum film thickness h_{min} at $S_a=10\%$, $\lambda=1\%$ and $U=1.2\text{m/s}$.

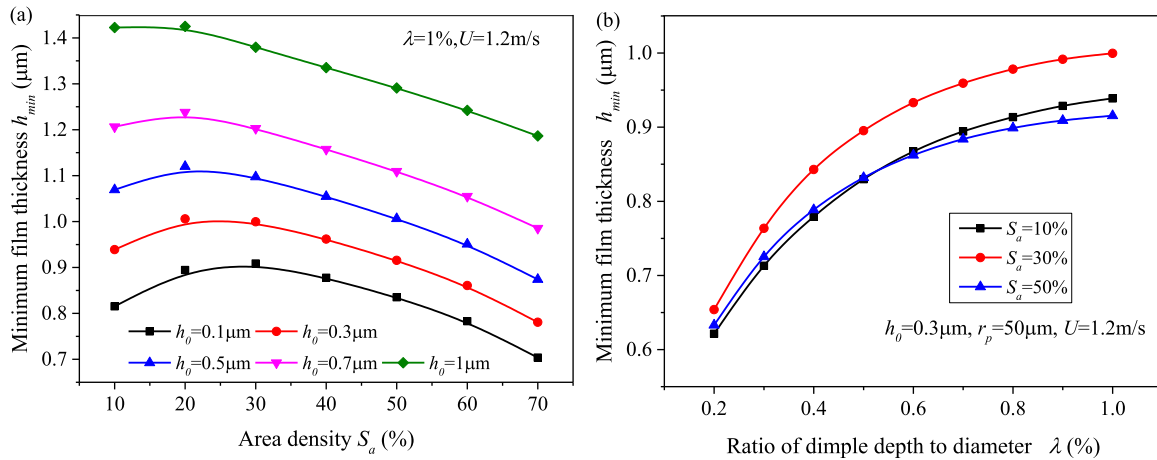


Fig. 13. Effect of the parameters of the surface texture on the minimum film thickness h_{min} .

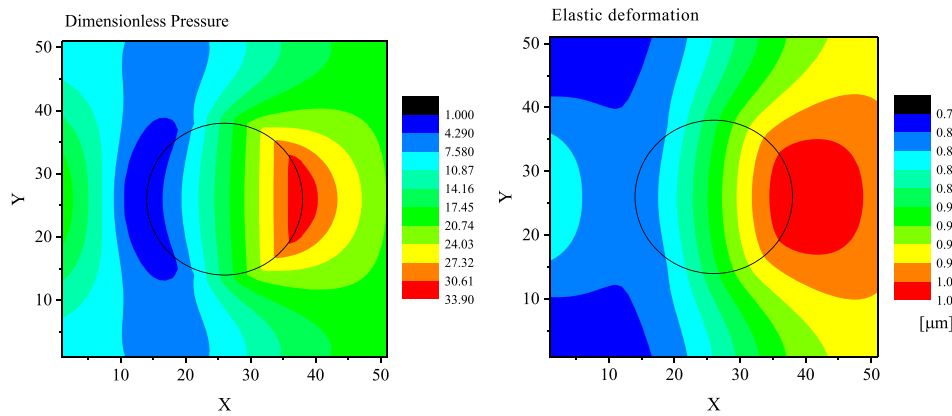


Fig. 14. Dimensionless pressure distribution and elastic deformation distribution of the textured surface at $h_0=0.1 \mu\text{m}$, $S_a=20\%$, $\lambda=1\%$ and $U=1.2 \text{ m/s}$.

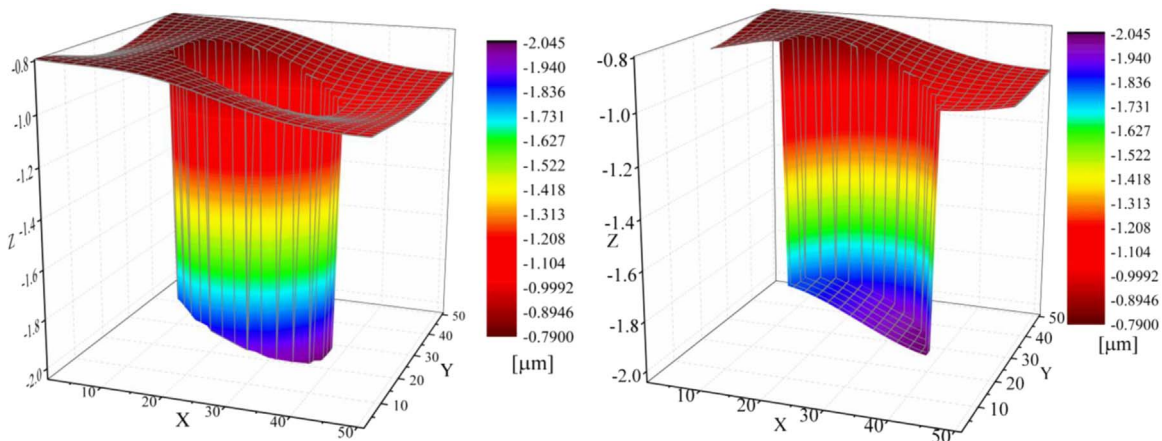


Fig. 15. The distorted textured surface of the center square cell at $h_0=0.1 \mu\text{m}$, $S_a=20\%$, $\lambda=1\%$ and $U=1.2 \text{ m/s}$.

density (see Fig. 18(f)).

It can be seen from Figs. 16–18 that the distribution of the dimensionless pressure and elastic deformation are basically echoed by each other and the max elastic deformations are all obtained in the zones where dimensionless pressures reach the peak. In addition, the effect of initial film thickness h_0 on the max values of dimensionless pressure and elastic deformation are well corresponding to that effect on the dimensionless average pressure P_{av} and average elastic deformation δ_{av} , respectively. This can be confirmed through comparing Figs. 4, 10 and 16. The same is true for the effect of the dimple depth-diameter ratio λ , however, the effect of area density S_a does not possess this characteristic.

The paper is numerically focused on the influence of elastic deformation on the load carrying capacity of fully textured parallel sliding bearings under hydrodynamic lubrication. It was found that elastic deformation could severely impact the load carrying capacity. In order to have more precise results, a more efficient mass-conserving approach suitable for the EHD solution is needed in future study. In addition, the conclusions drawn from this study may be limited to the full texture pattern. Dobrica [37] and Woloszynski's [38] research groups have respectively demonstrated that the spatial arrangement of dimples could severely influence the hydrodynamic effect and inertia effect of the textured sliding bearings. The effect of the spatial arrangement of dimples should be included in future study.

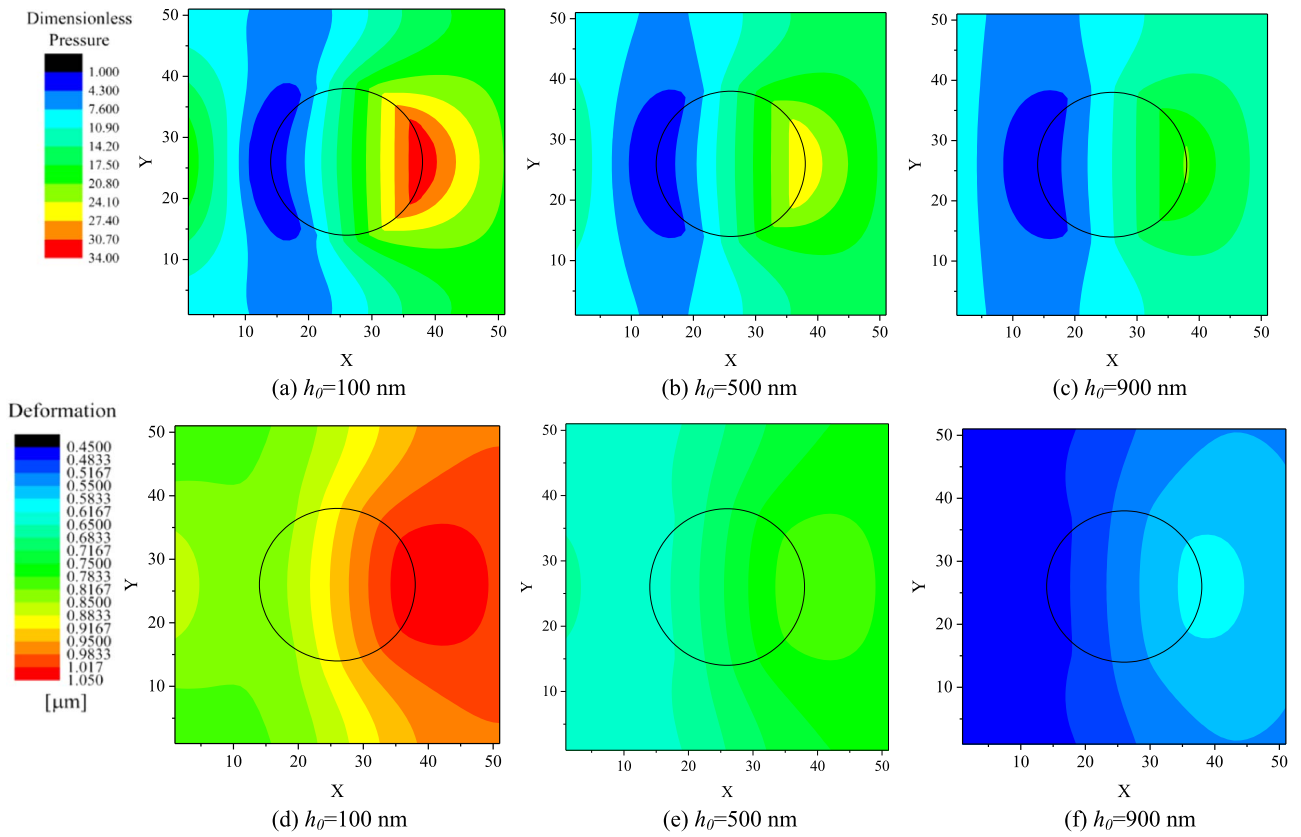


Fig. 16. Dimensionless pressure and elastic deformation distribution for various initial film thickness at $S_a=20\%$, $\lambda=1\%$ and $U=1.2$ m/s.

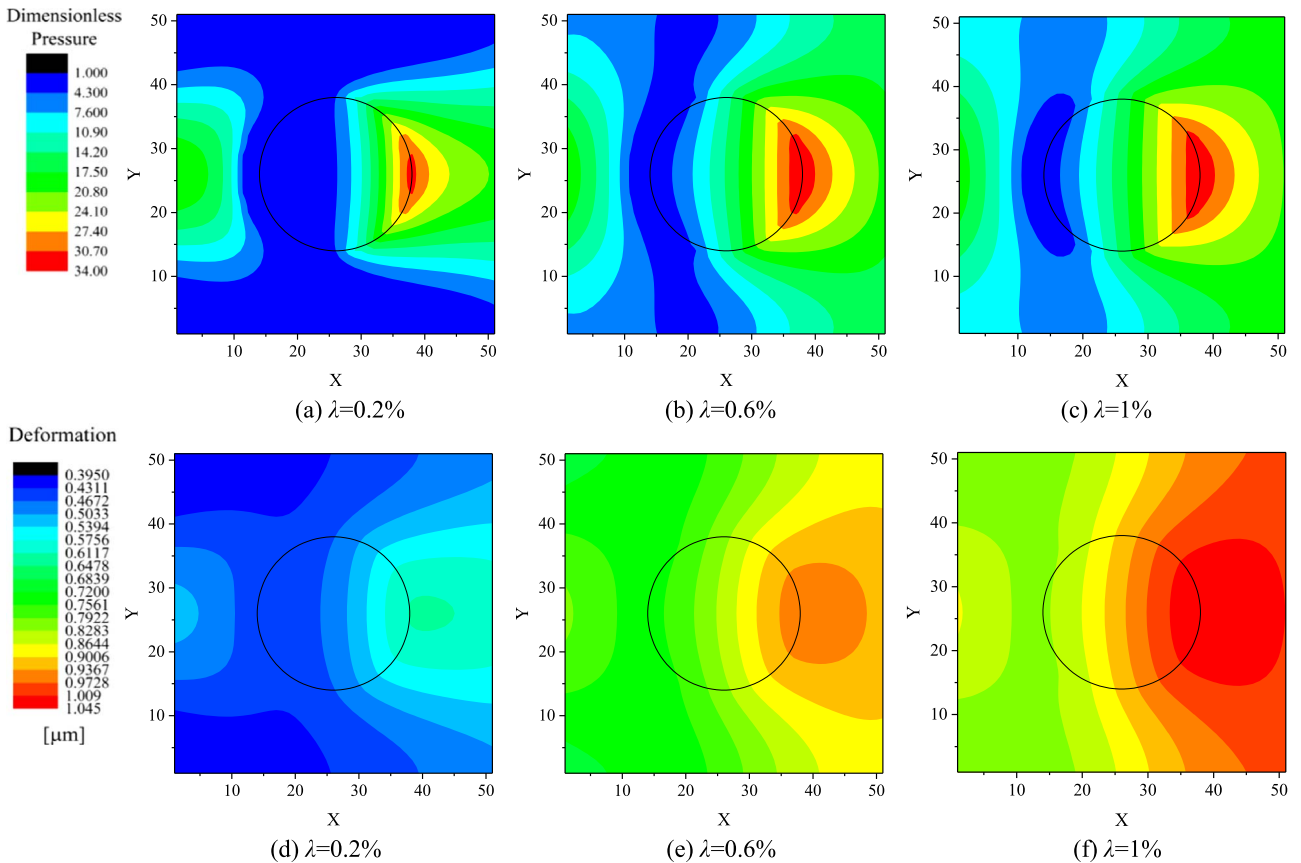


Fig. 17. Dimensionless pressure and elastic deformation distribution for various dimple depth at $h_0=0.1$ μm , $S_a=20\%$ and $U=1.2$ m/s.

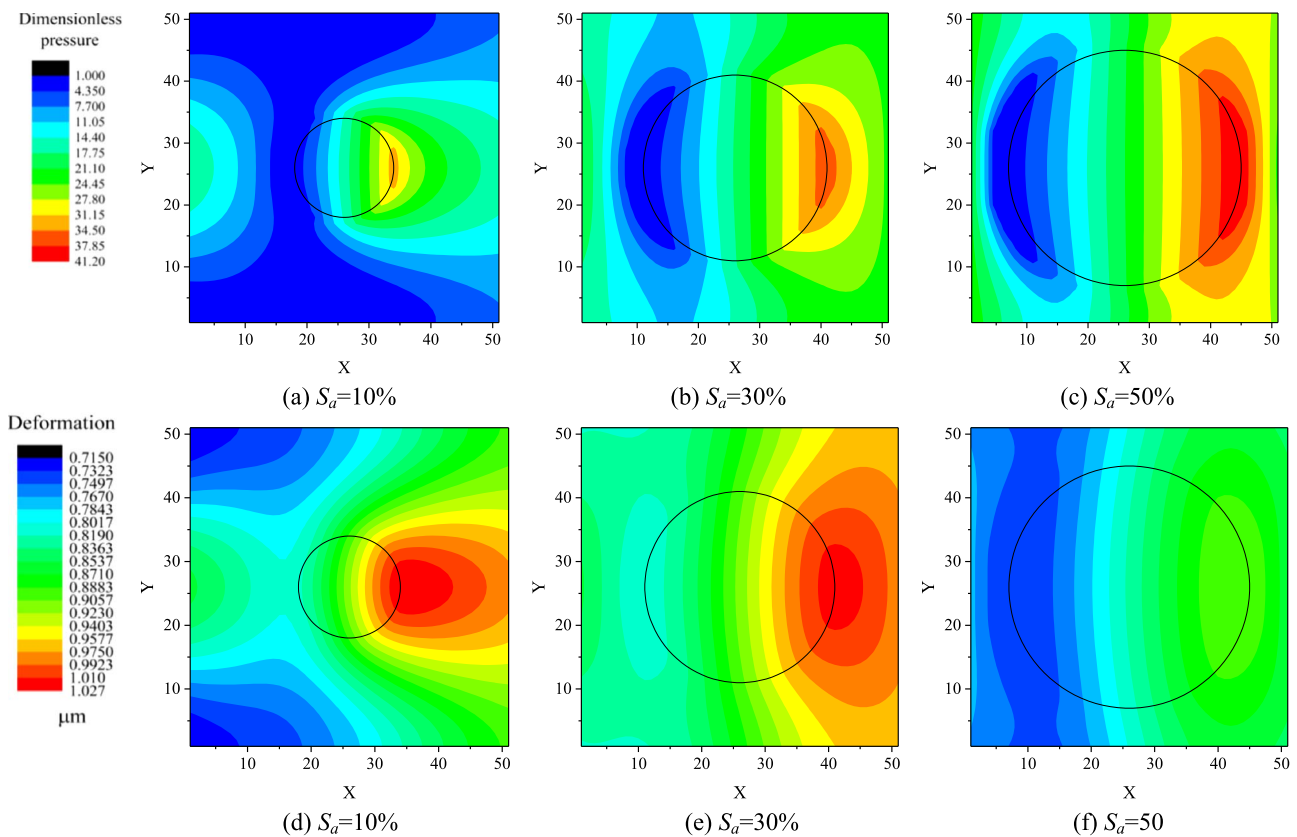


Fig. 18. Dimensionless pressure and elastic deformation distribution for various dimple area density at $h_0=0.1 \mu\text{m}$, $\lambda=1\%$ and $U=1.2 \text{ m/s}$.

4. Conclusions

A two-dimensional elastohydrodynamic numerical simulation is conducted for surface textured sliding bearings in thin film hydrodynamic lubrication, and the small elastic deformation of textured surface is investigated in detail. The following are the key conclusions drawn from the present study:

1. The small elastic deformation in thin film hydrodynamic lubrication have a significant negative influence on the maximum value and distribution of the film pressure, but when the initial film thickness $h_0 \geq 2 \mu\text{m}$ (Fig. 4), the effect of elastic deformation on lubrication property can be ignored.
2. In thin film hydrodynamic lubrication, the elastic deformation of the surface leads to the decrease of pressure peak and the increase of film thickness (Fig. 12), and results in that load carrying capacity becomes insensitive to area density S_a (Fig. 6), dimple depth-diameter ratio λ (Fig. 8) and sliding velocity U (Fig. 5) compared with the rigid solution.
3. Elastic deformation reprioritizes the texture parameters that influence the load carrying capacity of sliding bearings. For rigid solution, load carrying capacity is most easily affected by dimple depth over diameter ratio λ , and then texture area density S_a . While for EHD solution, the reverse is true, texture area density S_a becomes the most influential parameter (Figs. 6 and 8).
4. Elastic deformation also changes the optimal textured parameters for sliding bearings in term of load carrying capacity (Figs. 7 and 8). For EHD solution, optimal area density S_a for surface texture on UHMWPE varies with the initial film thickness h_0 , when $h_0 \leq 0.5 \mu\text{m}$, optimal value of S_a is 50%, in the range of $h_0=0.5-1 \mu\text{m}$, optimal value of S_a is 40%, when for $h_0 > 1 \mu\text{m}$, optimal value of S_a is 20%. But for rigid solution, the optimal value of S_a is 10% in most cases except when $h_0=0.1 \mu\text{m}$, in which the optimal value of S_a is 30%, under the simulation conditions of this study. As far as dimple

depth-diameter ratio λ , for EHD solution, a higher value is better; for rigid solution, lower is better.

Acknowledgements

This paper is based on the research work supported by the National Nature Science Foundation of China (NSFC) (No. 51675268).

References

- [1] I. Etsion, L. Burstein, A model for mechanical seals with regular microsurface structure, *Tribol Trans* 39 (3) (1996) 677–683.
- [2] C. Ma, H. Zhu, An optimum design model for textured surface with elliptical-shape dimples under hydrodynamic lubrication, *Tribol Int* 44 (9) (2011) 987–995.
- [3] A. Ramesh, W. Akram, S.P. Mishra, A.H. Cannon, A.A. Polycarpou, W.P. King, Friction characteristics of microtextured surfaces under mixed and hydrodynamic lubrication, *Tribol Int* 57 (2013) 170–176.
- [4] A. Bounif, M. Fillon, P. Maspeyrot, N. Tala-Ighil, Effects of surface texture on journal-bearing characteristics under steady-state operating conditions, *Proc Inst Mech Eng Part J: J Eng Tribol* 221 (6) (2007) 623–633.
- [5] X.L. Wang, K. Kate, K. Adachi, The effect of laser texturing of SiC surface on the critical load for transition of water lubrication mode from hydrodynamic to mixed, *Tribol Int* 34 (10) (2001) 703–711.
- [6] D. Gropper, L. Wang, T.J. Harvey, Hydrodynamic lubrication of textured surfaces—a review of modeling techniques and key findings, *Tribol Int* 94 (2016) 509–529.
- [7] T. Ibatan, M.S. Uddin, M.A.K. Chowdhury, Recent development on surface texturing in enhancing tribological performance of bearing sliders, *Surf Coat Technol* 272 (2015) 102–120.
- [8] V. Brizmer, Y. Kligerman, I. Etsion, A laser surface textured parallel thrust bearing, *Tribol Trans* 46 (3) (2003) 397–403.
- [9] T. Nanbu, N. Ren, Y. Yasuda, D. Zhu, Q.J. Wang, Micro-textures in concentrated conformal-contact lubrication: effects of texture bottom shape and surface relative motion, *Tribology Lett* 29 (3) (2008) 241–252.
- [10] R. Rahmani, I. Mirzaee, A. Shirvani, H. Shirvani, An analytical approach for analysis and optimisation of slider bearings with infinite width parallel textures, *Tribol Int* 43 (8) (2010) 1551–1565.
- [11] H. Yu, X. Wang, F. Zhou, Geometric shape effects of surface texture on the generation of hydrodynamic pressure between conformal contacting surfaces, *Tribology Lett* 37 (2) (2010) 123–130.
- [12] H. Yu, H. Deng, W. Huang, X. Wang, The effect of dimple shapes on friction of parallel surfaces, *Proc Inst Mech Eng Part J: J Eng Tribol* 225 (8) (2011) 693–703.

- [13] J. Han, L. Fang, J. Sun, Y. Wang, S. Ge, H. Zhu, Hydrodynamic lubrication of surfaces with asymmetric microdimple, *Tribol Trans* 54 (4) (2011) 607–615.
- [14] C. Shen, M.M. Khonsari, Numerical optimization of texture shape for parallel surfaces under unidirectional and bidirectional sliding, *Tribol Int* 82 (2015) 1–11.
- [15] M. Fesanghary, M.M. Khonsari, On the optimum groove shapes for load-carrying capacity enhancement in parallel flat surface bearings: theory and experiment, *Tribol Int* 67 (2013) 254–262.
- [16] I. Etsion, G. Halperin, V. Brizmer, Y. Kligerman, Experimental investigation of laser surface textured parallel thrust bearings, *Tribol Lett* 17 (2004) 295–300.
- [17] I. Etsion, Improving tribological performance of mechanical components by laser surface texturing, *Tribol Lett* 17 (4) (2004) 733–737.
- [18] X.L. Wang, K. Kate, K. Adachi, K. Aizawa, Loads carrying capacity map for the surface texture design of SiC thrust bearing sliding in water, *Tribol Int* 36 (3) (2003) 189–197.
- [19] X. Wang, K. Adachi, K. Otsuka, K. Kato, Optimization of the surface texture for silicon carbide sliding in water, *Appl Surf Sci* 253 (3) (2006) 1282–1286.
- [20] L. Bai, Y. Meng, V. Zhang, Experimental study on transient behavior of cavitation phenomenon in textured thrust bearings, *Tribol Lett* 63 (2016) 2.
- [21] J. Zhang, Y. Meng, Direct observation of cavitation phenomenon and hydrodynamic lubrication analysis of textured surfaces, *Tribol Lett* 46 (2) (2012) 147–158.
- [22] B. Zhang, W. Huang, X. Wang, Biomimetic surface design for ultrahigh molecular weight polyethylene to improve the tribological properties, *Proc Inst Mech Eng Part J: J Eng Tribol* 226 (8) (2012) 705–713.
- [23] B. Zhang, W. Huang, J. Wang, X. Wang, Comparison of the effects of surface texture on the surfaces of steel and UHMWPE, *Tribol Int* 65 (2013) 138–145.
- [24] X. Wang, J. Wang, B. Zhang, W. Huang, Design principles for the area density of dimple patterns, *Proc Inst Mech Eng Part J: J Eng Tribol* 229 (4) (2015) 538–546.
- [25] I. Etsion, Modeling of surface texturing in hydrodynamic lubrication, *Friction* 1 (3) (2013) 195–209.
- [26] K. Yagi, J. Sugimura, Elastic deformation in thin film hydrodynamic lubrication, *Tribol Int* 59 (2013) 170–180.
- [27] K. Yagi, J. Sugimura, Elastohydrodynamic simulation of Rayleigh step bearings in thin film hydrodynamic lubrication, *Tribol Int* 64 (2013) 204–214.
- [28] A. Shinkarenko, Y. Kligerman, I. Etsion, The effect of surface texturing in soft elasto-hydrodynamic lubrication, *Tribol Int* 42 (2) (2009) 284–292.
- [29] A. Shinkarenko, Y. Kligerman, I. Etsion, The effect of elastomer surface texturing in soft elasto-hydrodynamic lubrication, *Tribol Lett* 36 (2) (2009) 95–103.
- [30] S. Timoshenko, J.N. Goodier, *Theory of elasticity*, 2nd ed., McGraw Hill, New York, 1951.
- [31] D. Dowson, D. Wang, Impact elastohydrodynamics, *Lubr Lubr* 30 (1995) 565–582.
- [32] M. Taniguchi, D. Dowson, C.M. Taylor, The effect of spin motion upon elastohydrodynamic elliptical contacts, *Elastohydrodynamics* 32 (1997) 599–610.
- [33] Y. Qiu, M.M. Khonsari, On the prediction of cavitation in dimples using a mass-conservative algorithm, *J Tribol* 131 (4) (2009) 041702.
- [34] Press WH, Teukolsky SA, Vetterling WT, Flannery BP. *Numerical Recipes in Fortran 77: The Art of Scientific Computing Vol 1 Second Edition*. Cambridge University Press.1992
- [35] K. Hou, D. Zhu, S. Wen, A new numerical technique for computing surface elastic deformation caused by a given normal pressure distribution, *J Tribol* 107 (1) (1985) 128.
- [36] I. Etsion, Y. Kligerman, G. Halperin, Analytical and experimental investigation of laser-textured mechanical seal faces, *Tribol Trans* 42 (3) (1999) 511–516.
- [37] M.B. Dobrica, M. Fillon, M.D. Pascovici, T. Cicone, Optimizing surface texture for hydrodynamic lubricated contacts using a mass-conserving numerical approach, *Proc Inst Mech Eng Part J: J Eng Tribol* 224 (8) (2010) 737–750.
- [38] T. Woloszynski, P. Podsiadlo, G.W. Stachowiak, Evaluation of inertia effect in finite hydrodynamic bearings with surface texturing using spectral element solver, *Tribol Int* 91 (2015) 170–176.